remote sensing

MDPI

Article

InSAR Monitoring Using Persistent Scatterer Interferometry (PSI) and Small Baseline Subset (SBAS) Techniques for Ground Deformation Measurement in Metropolitan Area of Concepción, Chile

Eugenia Giorgini [1,2], Felipe Orellana [3,*], Camila Arratia [4], Luca Tavasci [1], Gonzalo Montalva [3], Marcos Moreno [5] and Stefano Gandolfi [1]

1 Department of Civil, Chemical, Environmental, and Materials Engineering—DICAM, University of Bologna, 40136 Bologna, Italy; eugenia.giorgini@unibo.it (E.G.); luca.tavasci@unibo.it (L.T.); stefano.gandolfi@unibo.it (S.G.)
2 National PhD in Earth Observation, Sapienza University of Rome, 00185 Rome, Italy
3 Department of Civil Engineering—DIC, University of Concepcion, Concepcion 4070371, Chile; gmontalva@udec.cl
4 Department of Geophysics—DGEO, University of Concepcion, Concepcion 4070386, Chile; carratia2017@udec.cl
5 Department of Structural and Geotechnical Engineering—DIEG, Pontifical Catholic University of Chile, Santiago 7820436, Chile; marcos.moreno@uc.cl
* Correspondence: felipeorellana@udec.cl

Abstract: InSAR capabilities allow us to understand ground deformations in large metropolitan areas, this is key to assessing site conditions in areas in an inherently expanding context. The multi-temporal interferometry of SAR data records ground surface displacement velocities over large metropolitan areas, identifying anomalous and potential geological hazards. The metropolitan city of Concepción, Chile, is an alluvial basin in one of the world's most seismically active subduction zones, where many subduction earthquakes have occurred throughout history. In this study, we monitored the deformations of the ground surface in the metropolitan area of Concepción using two interferometric techniques, the first being Persistent Scatterer Interferometry (PSI) and the second, the Small Baseline Subset (SBAS) technique. To do this, we have used the same Sentinel-1 dataset, obtaining ground movement rates between 2019 and 2021. The velocities were aligned with the GNSS station available in the area. Ground deformation patterns show local deformations depending on factors such as soil type and heterogeneity, and regional deformations due to geographical location in the subduction area. Our results highlight the similarity of the deformation rates obtained with different processing techniques and have also allowed us to identify areas of deformation and compare them to site conditions. These results are essential to evaluate ground conditions and contribute to urban planning and risk management in highly seismic areas.

Keywords: InSAR; ground deformation; SBAS; PSI; Sentinel-1

Citation: Giorgini, E.; Orellana, F.; Arratia, C.; Tavasci, L.; Montalva, G.; Moreno, M.; Gandolfi, S. InSAR Monitoring Using Persistent Scatterer Interferometry (PSI) and Small Baseline Subset (SBAS) Techniques for Ground Deformation Measurement in Metropolitan Area of Concepción, Chile. *Remote Sens.* **2023**, *15*, 5700. https://doi.org/10.3390/rs15245700

Academic Editors: Cristiano Tolomei and Michele Saroli

Received: 19 October 2023
Revised: 24 November 2023
Accepted: 8 December 2023
Published: 12 December 2023

1. Introduction

Monitoring land changes and ground deformation from techniques based on Synthetic Aperture Radar (SAR) is extremely important to identify hazards in built environments and infrastructures, especially in urban areas exposed to large seismic threats [1–3]. Among the various monitoring methods, multi-temporal interferometric Synthetic Aperture Radar (InSAR) has been used since the 2000s [4,5]. The technique consists of processing a long dataset of SAR images of the same area of interest, collected over a period of time via satellite observation. From the processing of the SAR dataset, it is possible to obtain useful information on velocity patterns and time series with centimeter to millimeter precision [6,7].

Multi-temporal InSAR's capabilities are its spatial and temporal coverage and remote monitoring at a consistent and continuous rate, making it suitable for monitoring large urban areas. This technique is mainly used in the field of geoscience to monitor the solid Earth's processes or phenomena that cause deformations, such as seismic deformation [8–10], volcanic, and landslides monitoring [11–13], and water withdrawals [14–16], as well as for infrastructure maintenance and monitoring tasks [17–20].

We can divide InSAR techniques that focus on addressing signal decorrelations to estimate atmospheric signals and deformations [21]. These techniques can be divided into two main approaches: First are Persistent Scatterers (PS) techniques, which identify coherent measurement points, recorded mainly in urban areas where there are buildings whose return signal is rarely overpowered by noise [22,23]. Several algorithms have been developed with the PS approach, e.g., [23–28] using coherent pixel selection criteria [20]. The second approach is the Small Subset Baseline (SBAS) technique, which compensates for the areas affected by the decorrelation of the SAR signal, thanks to the network of redundant interferograms [4,29]. SBAS is based on multi-look images and may not be suitable for studying local-scale deformations [4]. This drawback has been overcome by extending the SBAS method to full spatial resolution data [29]. Many algorithms have been developed using SBAS techniques, e.g., [30–32]. Recently, a parallel SBAS (P-SBAS) algorithm was developed to allow for the processing of large amounts of InSAR data [33,34].

The Copernicus program of the European Space Agency (ESA) allows us to obtain continuous and open access SAR data from the Sentinel-1 mission, which consists of two twin satellites [35]. Sentinel-1 satellites, of which one has been active since 2014 and the other since 2016have created an extensive database of SAR acquisitions in recent years, which are available to users and can be used for monitoring by Earth Observation (EO) techniques. these satellites provide different types of products depending on the acquisition mode used. In particular, acquisition based on progressive scanning terrain observation [36] were used for the present study. One of the most important features of the Sentinel-1 satellites is the significant improvement in the revisit time of the same area compared to previous European C-band SAR missions, reduced from 35 to 6 days. Another main feature is the Terrain Observation with Progressive Scans SAR (TOPSAR) acquisition mode, which allows us to select small urban areas of interest through bursts and swaths. Several studies have addressed Sentinel-1 SAR interferometry in different applications.

InSAR measurements allow us to record and quantify ground displacement, from which time series it is possible to evaluate the mean annual rate of the movement. The measurements are made along the line connecting the sensor and ground targets, called the sensor line of sight (LOS). However, in the post-processing phase, there is the possibility, by using ascending and descending orbits, of determining the surface movements that generally occur in the horizontal (E-W) and vertical (UP) directions. For the correct use of the information obtained from InSAR processing, its quality must be evaluated with precision and accuracy. The former is usually identified in terms of the standard error of the displacement velocities [37], which depends on the quality of the scatterers, in terms of coherence [38–40]. The accuracy of the measurements is usually compared to geodetic instruments (e.g., GNSS), indicating the errors of the relative InSAR estimates against the absolute GNSS measurements; however, there are SAR instrument calibration methods, in some cases, in phase processing, and in others, for the correction of measurements.

This study aims to assess the potential and limitations of differential InSAR processing techniques based on Sentinel-1 images, particularly in the study case of deformations that affect urban areas exposed to natural subduction. The research focuses on the use of the main coherence-based multi-temporal InSAR processing approaches: the Small Baseline Subset (SBAS) [4] and the StaMPS [23] methods. The results have been compared and analyzed, mainly considering the mean velocities along the LOS and UP directions, as well as E-W. The results are interpreted according to the geological conditions of the area of interest. Based on the seismotectonic context, the study area is in the subduction area of the Nazca plate beneath the South American plate. In addition, an estimation of site

conditions was carried out using microtremors in the urban environment. By processing these measurements, we have been able to identify the different predominant frequencies in soils with areas prone to significant deformation on the surface of the urban area of Concepción. Numerous seismic events have affected the subduction segment associated with the study area. Therefore, a fundamental evaluation of the conditions of the area is fundamental for the prevention and mitigation of threats in the urban area is also provided.

Seismotectonic and Geological Setting

The study area is the basin of the metropolitan city of Concepción, located in the Chilean subduction zone, which has permanent seismic activity, which contributes to local deformations of civil infrastructure. The Concepción basin is in the Chilean coastal mountain range in the southern segment of the subduction zone, particularly in the area covering the rupture of the large Mw 8.8 Maule earthquake of 2010 (Figure 1). The urban area velocities from GNSS observations between 2018 and 2021 show typical patterns of interseismic deformation (Figure 1). In addition, it moved towards the northeast with magnitudes of ~20.00 mm/year near the coast, decreasing to ~10.00 mm/year towards the Andes Mountain range.

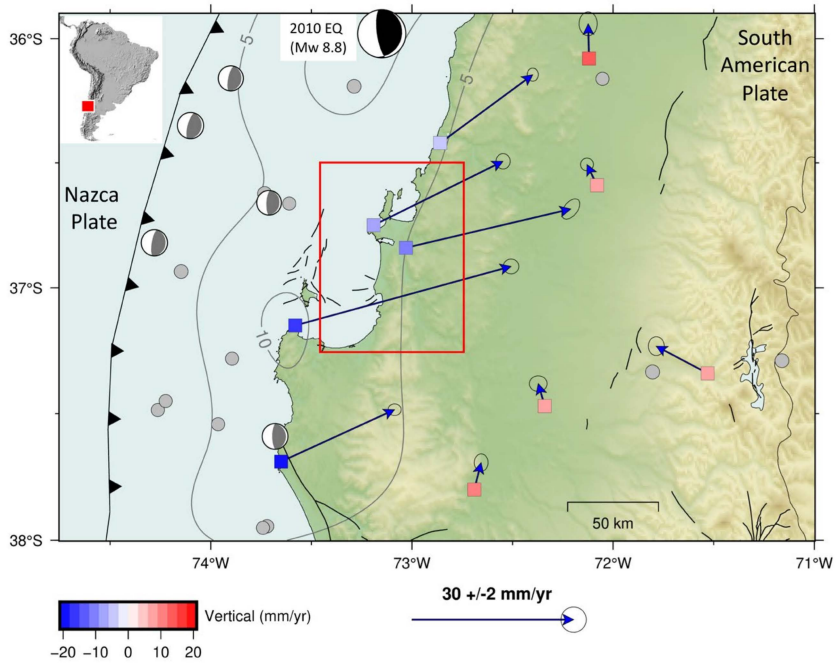

Figure 1. Map of a segment of subduction in south-central Chile. The study area is indicated by the red box. The configuration of the Nazca and South American plates, the rupture zone of the 2010 earthquake [41] and its focal mechanism are shown. Circles indicate seismic events of magnitude greater than Mw 6 that have occurred from 2010 to the present. Also shown are the focal mechanisms of earthquakes greater than magnitude 6.5 in the same period. The GNSS velocity field is shown in Yañez-Cuadra et al. [42]. The blue arrows indicate the horizontal GNSS velocities. The squares show the GNSS-derived vertical displacements.

The geological formations of the study area are Pleistocene to Holocene sediments that filled the river basin [43]. This structure is associated with a set of NE-oriented normal faults that cut and displaced the bedrock formed by Cretaceous sedimentary rocks [44,45]. The basin fill is dominated by sandy fluvial terraces formed by the meanderings of the Biobío River [43]. This process deposited a homogeneous unit composed of metric banks of well-selected sand grains [45]. The main geological units of the area are shown in Figure 2 and are described below.

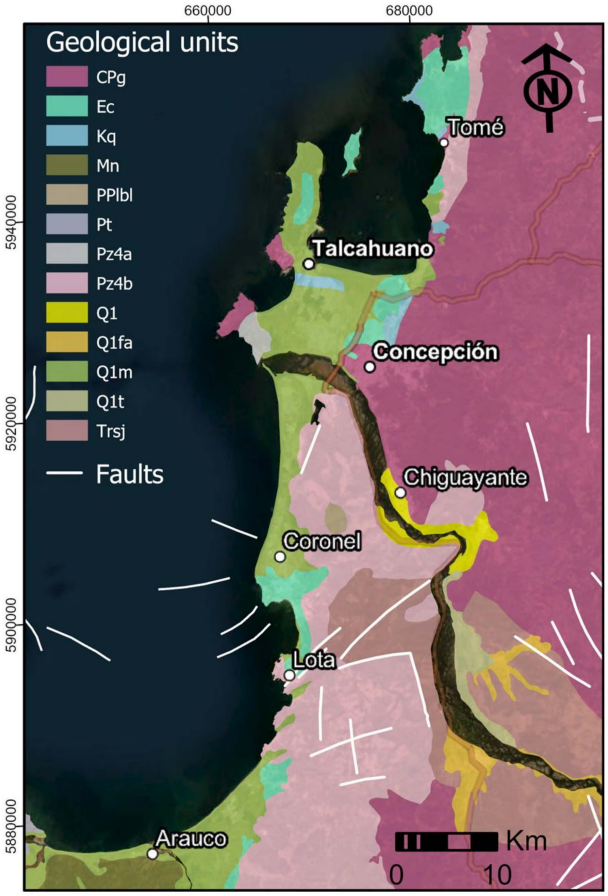

Figure 2. Geological units in area of interest defined in [46]. Key features include CPg (undifferentiated tonalites and granodiorites), Ec (sandstones and clays with coal seams), Kg (conglomerates and marine sandstones—Senonian), Mn (tuffaceous sandstones and marine siltstones), PPlbl (conglomeratic to breccia cinerites with clasts and volcanic matrix), Pt (marine sandstones and siltstones), Pz4a (micaschists and metacherts), Pz4b (meta-morphic basement—slates, phyllites, and metasandstones), Q1 (current valley sediments), Q1fa (gravels, rubble, and sand generated in paleochannels), Q1m (sand and fine sediment deposits), Q1t (gravels, sand, and fine sediments), Trsj (sequences of continental and marine shales, sandstones, lavas, and andesitic breccias).

2. InSAR Techniques Methods

In this study, we used a common dataset with two different InSAR implementations. Firstly, a medium-resolution dataset in meters (90 range × 90 azimuth) using the Small Baseline Subset (SBAS) approach [4] was used. Subsequently, a full-resolution dataset in meters (5 range × 20 azimuth) based on the Persistent Scatterer Interferometry (PSI) approach [5] through the StaMPS software was used. Both processing algorithms use Single Look Complex (SLC) interferometric products acquired in Terrain Observation with the Progressive Scans SAR (TOPSAR) acquisition mode from the Sentinel-1 satellites. The processing chains were applied using the same SAR scenes from May 2019 to May 2021. The following presents some details about the dataset and basic remarks on the theoretical aspects of the two investigated approaches.

2.1. SAR Data

The dataset consists of 60 ascending and 60 descending SAR images from the Sentinel-1A–1B, operating in the C-band with a frequency/wavelength of 5.405 GHz/5.5 cm. The satellite observation period from May 2019 to May 2021 is considered sufficient to detect spatiotemporal changes on the ground surface. We used both orbits of the Sentinel-1 satellites, ascending and descending (Table 1), for which the data are available at the

HUB of the Copernicus program of the European Space Agency (ESA). The collection of Sentinel-1A–1B data was limited to the observation period with a 6-day revisit time. The interferometric product for the Sentinel-1 sensor was acquired as a Single Look Complex (SLC), using Interferometric Wide Swath (IW) and the TOPSAR mode [47], which allowed us to optimize performance in both PSI and SBAS processing, through specific IW and bursts, over the area of interest (AOI).

Table 1. SAR data features.

Orbit	Ascending	Descending
Sensor	Sentinel-1A–1B	Sentinel-1A–1B
N° acquisition	60	60
Start date	05/05/2019	05/05/2019
End date	05/05/2021	05/05/2021
Orbit	86	156
Polarization	VV	VV
Swath	IW2	IW2–IW3
Bursts	4–6	5–7

2.2. PSI Techniques

The PSI technique has been used, implementing the Stanford Method for Persistent Scatterers (StaMPS) algorithm [23]. This technique selects Persistent Scatterers (PS) and exploits spatial correlation [48]. Consequently, it identifies dim scatterers with a lower Signal-to-Clutter (SCR) and provides denser target coverage, even in natural coverage [49,50]. The interferometric processing is based on the implementation of an open source toolbox, involving two main steps: (i) the automatic generation of interferograms in the Sentinel Applications Platform (SNAP), and (ii) PS processing and time series generation using StaMPS (see Figure 3).

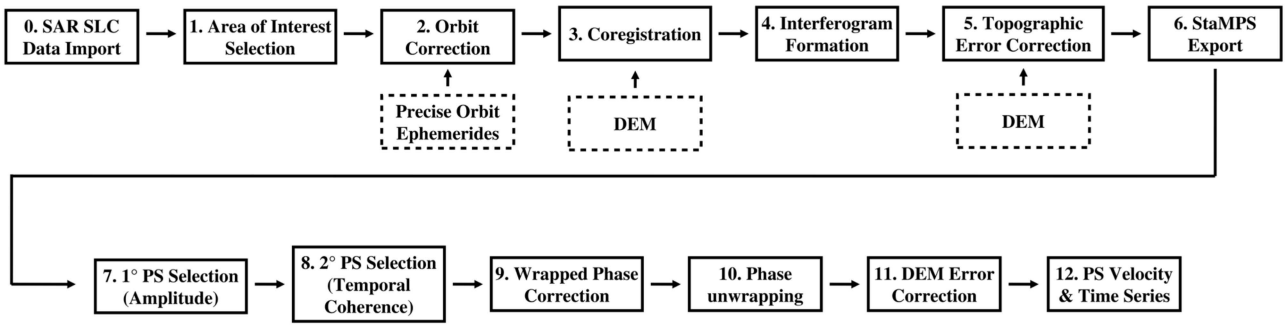

Figure 3. StaMPS workflow processing for PSI technique.

Step I involves SNAP processing, performed using the Python script and the processing graphs of the Snap2stamps repository [48,51]. Using the Snap2stamps package is fundamental, as the scripts optimize time and resources. The automatic processing scheme performs six main steps: data import, the selection of the area of interest, the correction of the orbital error, coregistration, interferogram formation, the correction of the topographic error, and StaMPS export. As one of the main differences to the SBAS approach, as described below, it is important to emphasize that the interferograms are formed according to the unique primary approach, i.e., from primary–secondary pairs (Figure 4). The primary acquisition is chosen in the middle of the considered time span, thus minimizing the temporal decorrelation which effects the interferogram's phase. The interferograms are formed by evaluating the differential phase between the primary acquisition and the other acquisitions of the stack.

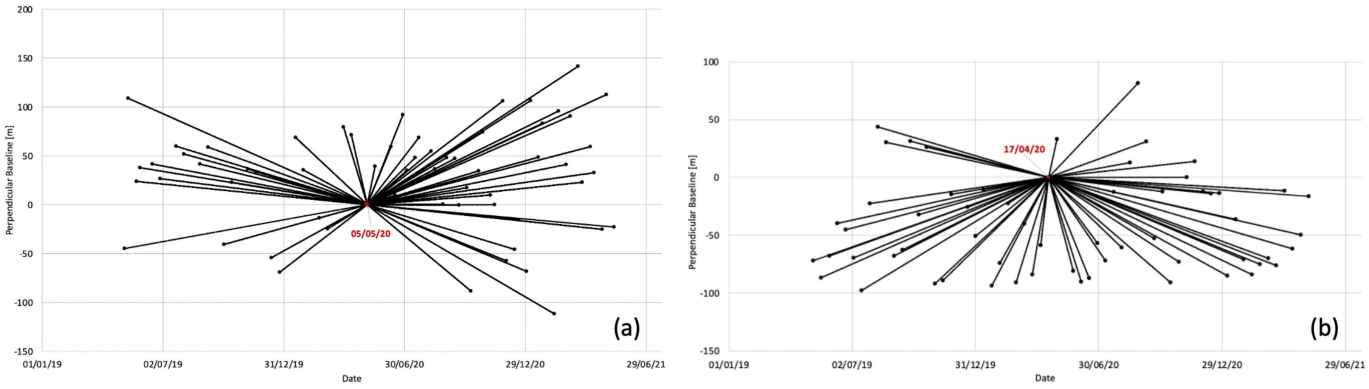

Figure 4. Interferometric pairs in the temporal/perpendicular baseline plane for PSI technique. (**a**) Ascending and (**b**) descending interferogram network.

Step II involves the input of SNAP exports into StaMPS using a specific script in Python. Then, the StaMPS PSI processing chain is executed in seven steps, as described in StaMPS [51]. The results of the implemented PSI processing are the displacement velocity of the Persistent Scatter (PS) pixels at known locations characterized by amplitude stability, phase stability, and high temporal coherence.

2.3. SBAS Technique

The SBAS technique is based on selecting many pairs of SAR images with small spatial and temporal separations [4,29,52]. The aim is to reduce the decorrelation phenomena afflicting the SAR images' phase [53]. This method allows multiple interferograms to be generated, compared to the single-primary approach implemented by PSI techniques, to mitigate noise and maximize target coherence. The time series are achieved by searching for a least squares solution [7]. For each coherent measurement point, the displacement time series and the average strain rate are recovered with millimeter precision [6].

SBAS processing was performed in an ESA GRID computing-based operating environment [54–57] on the GEP platform, using a parallelized SBAS algorithm. The P-SBAS approach was configured for Sentinel-1 IW TOPS data processing [34,55] (Figure 5). The pairs of acquisitions were identified following the constraints imposed by [52] (Figure 6). In addition, the SBAS processing chain includes a multi-look operation during coregistration at step 4 to mitigate the effects of decorrelation noise. This spatial average increases pixel size, from about 5 × 20 mt to about 90 × 90 mt. The results of the SBAS processing are stable pixels, characterized by high temporal coherence, with known location, velocity, and time series.

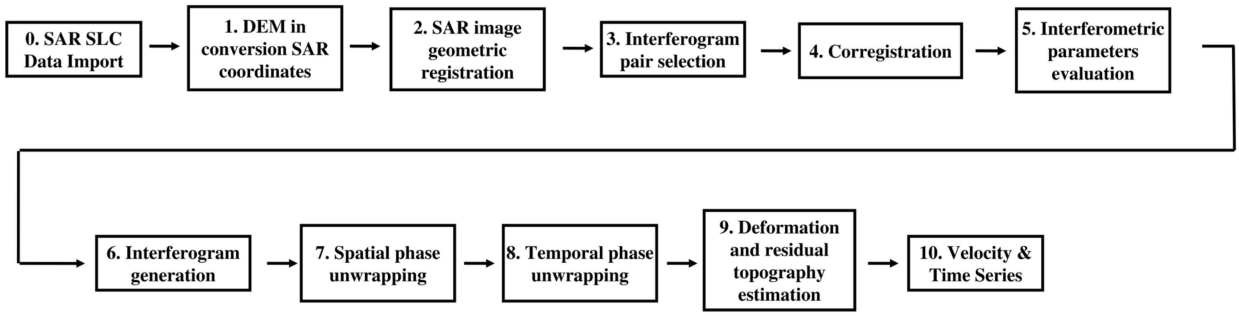

Figure 5. SBAS workflow processing.

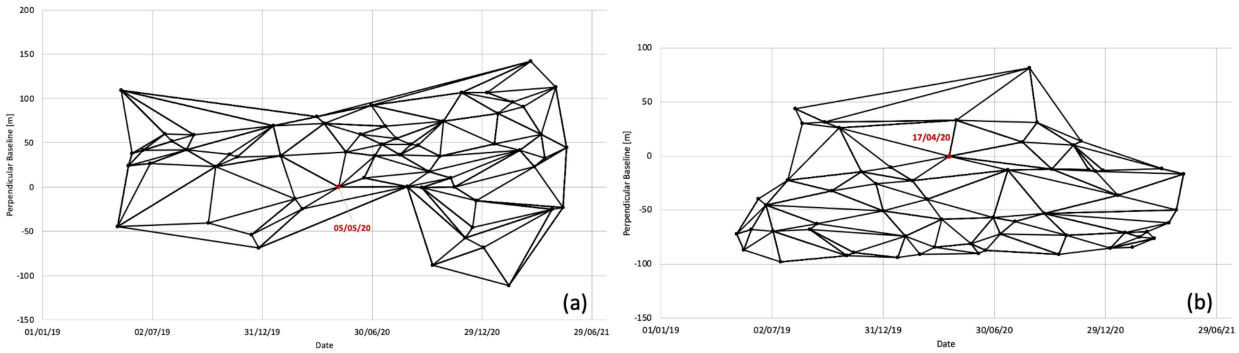

Figure 6. Interferometric pairs in the temporal/perpendicular baseline plane for SBAS technique. (**a**)Ascending and (**b**) descending interferogram network.

2.4. Post-Processing and Measurements Correction

Since the InSAR velocities estimated on the defined PS are inherently coherent but not aligned to a well-defined reference frame, it is fundamental in a post-processing phase to align these results using a geodetic ground reference such as leveling benchmarks or permanent GNSS stations. This procedure is the so-called calibration of the InSAR data and consists of switching from a local, geometry-dependent geodetic reference system of the SAR satellite images acquisitions to an absolute geodetic reference system. For this study, the calibration is carried out using the GNSS coordinates of the HLPN GNSS permanent station [58], which were aligned to the absolute International Terrestrial Reference Frame [59]. The SAR datum represents a relative movement of an area, unconstrained by the ground truth, and that needs to be calibrated and validated [60,61]. To calibrate both the SBAS and PSI backscatterers obtained, the HLPN positions were projected along the LOS directions. This operation was carried out by applying the decomposition matrix containing the incidence angles and the heading angles unique for each acquisition geometry, as described in [62]. The HLPN time series projected in the NEU reference and along the LOS direction are reported in Figure 7. The recorded period is from 2016 to 2022, with 21.60 mm/year in the northern direction, 23.30 mm/year in the eastern direction, and −12.00 mm/year in the UP direction (Figure 7). The displacement velocity along the LOS direction are, respectively, −22.50 mm/year and 4.60 mm/year for the ascending and descending geometries (Figure 7b).

The PSI results were aligned to the ITRS reference system by computing the velocity difference along the LOS between HLPN and the closest InSAR PS, then subtracting this difference from all other PSs separately for both ascending and descending acquisition geometries. As for the SBAS data, it has not been possible to directly couple a PS to the GNSS station since that area was clipped out from the SAR processing on the GEP platform. Therefore, we aligned the SBAS by subtracting from all PSs the average value of the differences between the SBAS velocities and the already aligned PSI velocities of all the PSs.

The vertical movements were obtained by combining the results from ascending and descending geometries, independent of the horizontal East–West components. The LOS velocities were combined by applying the decomposition matrix described in [63] for each pair of commonly located PSs. As for the SBAS data, this was simplified by the fact that PSs were already geometrically aligned on the same 90 × 90 m grid. Differently, for the PSI techniques, it was necessary to choose a criterion to link commonly located PSs from the two LOS directions. In this case, we set a 20 × 20 m grid and averaged the velocities of all the PSs within each cell, both for the ascending and descending geometries. These averaged values were then decomposed to estimate vertical (UP) and horizontal (Eastern) velocities.

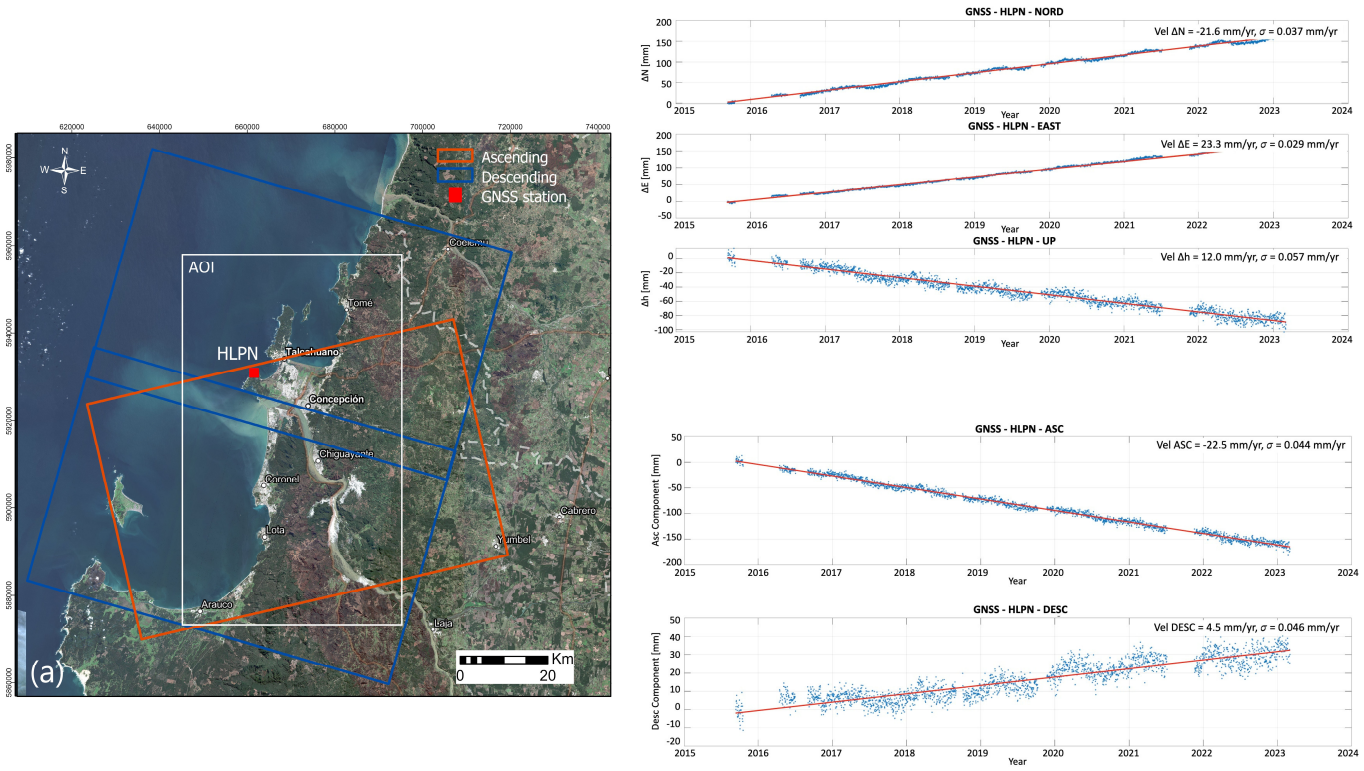

Figure 7. (**a**) Area of interest (AOI), frames for ascending and descending orbits, and (**b**) GNSS time series HLPN station (blue dots) with regression lines (red).

Finally, for a direct comparison of velocities obtained from the SBAS and PSI approaches, the PSI outcomes were interpolated over the same 90 × 90 m grid used for SBAS. This interpolation was carried out before the velocity decomposition along the line of sight (LOS) direction and after the decomposition along the UP and east–west directions.

3. Results and Discussions

This section reports the main result obtained by the InSAR data in terms of ground deformation phenomena, together with some comparison between the two processing methods utilized. LOS deformation maps are presented for both PSI and SBAS techniques. In both cases, the target points (pixels) are relevant for measuring deformation in urban areas, making it possible to record the displacement velocity on a tectonic scale and to measure the deformations in local areas, in addition to discussing the potential and limitations of both techniques. Subsequently, estimations of the vertical (UP) and horizontal (E-W) displacement components are provided. Finally, an overview of the seismological and geotechnical characterization of the inspected area is presented, complemented by details on the local geology and microvibration measurements.

3.1. Ground Deformation Measurements

Figure 8 shows the mean displacement velocities estimated using the two InSAR approaches for each LOS measurement point in ascending and descending geometries. The values were classified according to a color scale, ranging from red to green for LOS velocity maps. These results were obtained before to calibrate the GNSS data. Negative velocity values (mm/year) indicate movement away from the satellite sensor, while positive velocity values indicate movement towards the sensor.

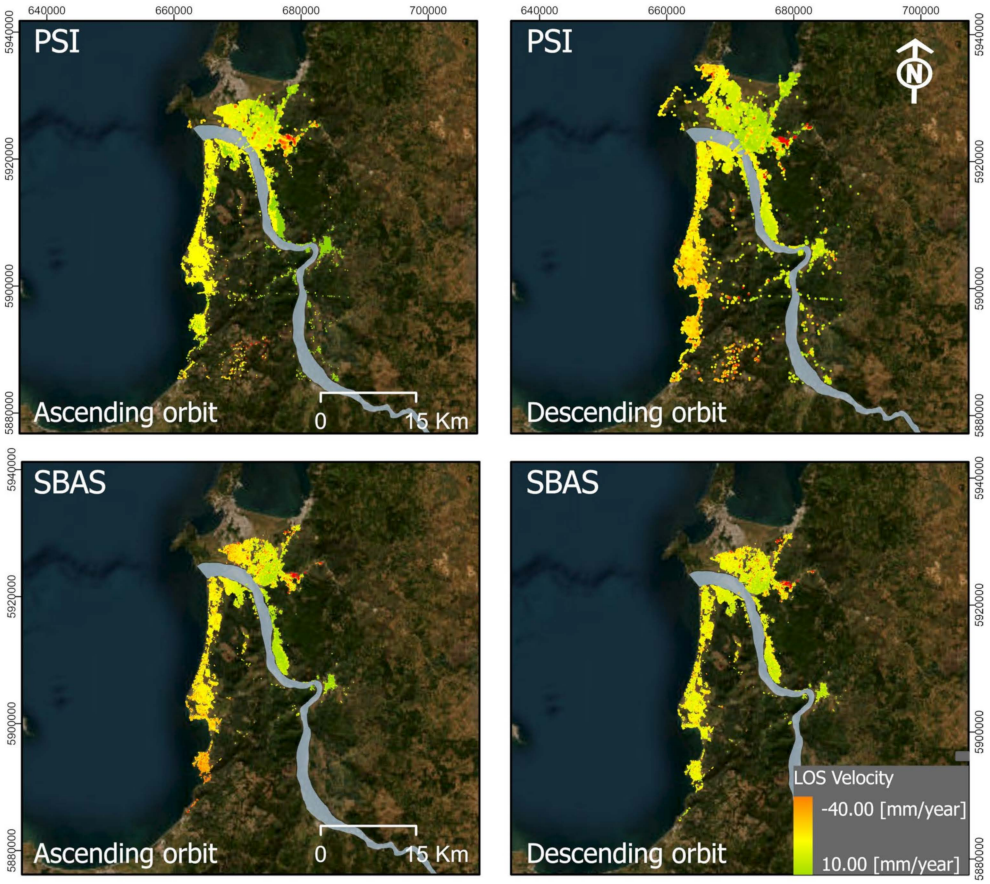

Figure 8. LOS velocities maps for SBAS and PSI techniques in area of interest (AOI) of Concepción, Chile, background maxar image. Source: Esri.

The results obtained using the SBAS technique have a spatial resolution of 90 × 90 m to the ground, resulting in the multi-look step implemented and described above [32]. However, these results have provided a high density of points, reaching 100 points/km^2 in the urban area (Figure 8). With the PSI technique, we used the maximum spatial resolution of 5 × 20 m in range and azimuth, respectively. Using the InSAR technique, the density of points over the urban area increased to 800 points/km^2. Several PS were also identified along bridges (Figure 8). Most stable areas are evidenced by light green dots, showing where velocities are close to zero, while red dots highlight areas undergoing deformations. By comparing the resulting velocities on a common grid after the calibration of GNSS data, some relatively small differences were found between the PSI and SBAS values. In particular, the standard deviation of the residuals is 1.40 mm/year for the descending geometry, while it reaches 2.80 mm/year for the ascending one. Point-to-point differences are up to the 1 cm level but only in few cases related to the ascending acquisition geometry. These point-to-point differences are due to the different selection of the Persistent Scatterers implemented by the two approaches, which makes the PSI results inherently more spatially resolute on the original grid but less sensitive when averaging the data over the 90 × 90 m grid considered in this comparison.

3.2. Vertical and East–West Displacements Analysis

The study area of Concepción, Chile, is an urban area exposed to dynamic terrestrial processes, as it is an area that is constantly under conditions of extreme fragility due to high seismic activity due to the influence of the active subduction margin. The vertical (UP) and horizontal (E-W) velocities estimations allow us to know the relief changes generated in the subduction area, such as the uplift or subsidence. The measurements of the deformations in the study area indicate the rates of vertical displacements (UP)

ranging from about −30.00 mm/year to −3.00 mm/year, and the negative displacements in red are accentuated in the subduction margin (Coronel, Lota). The two relatively large anomalous subsidence domains are associated with the tectonic activity of the area. On the contrary, local deformations occur in fine sediments of lacustrine origin, which are part of Biobío River delta formation, which was favored by large quantities of Andean sediments transported and defined by the climate and sea level [64]. The horizontal or East velocity rates range from 8.00 mm/year to 38.00 mm/year (Table 2, Figure 9). These values are strongly affected by the tectonic drift introduced in the calibration phase by using the ITRS reference system to express the GNSS velocity, which are about 20.00 mm/year along the eastern direction.

Table 2. UP and East velocity trends for SBAS and PSI techniques, resampled for differently spaced grids.

Technique (Range × Azimuth)	UP Velocity (mm/year) (min | mean | max)	East Velocity (mm/year) (min | max)
SBAS (90 × 90 mt)	−27.69 | −12.31 | −3.82	8.10 | 23.01 | 38.70
PSI (20 × 20 mt)	−25.12 | −12.27 | −5.60	9.30 | 23.56 | 35.11

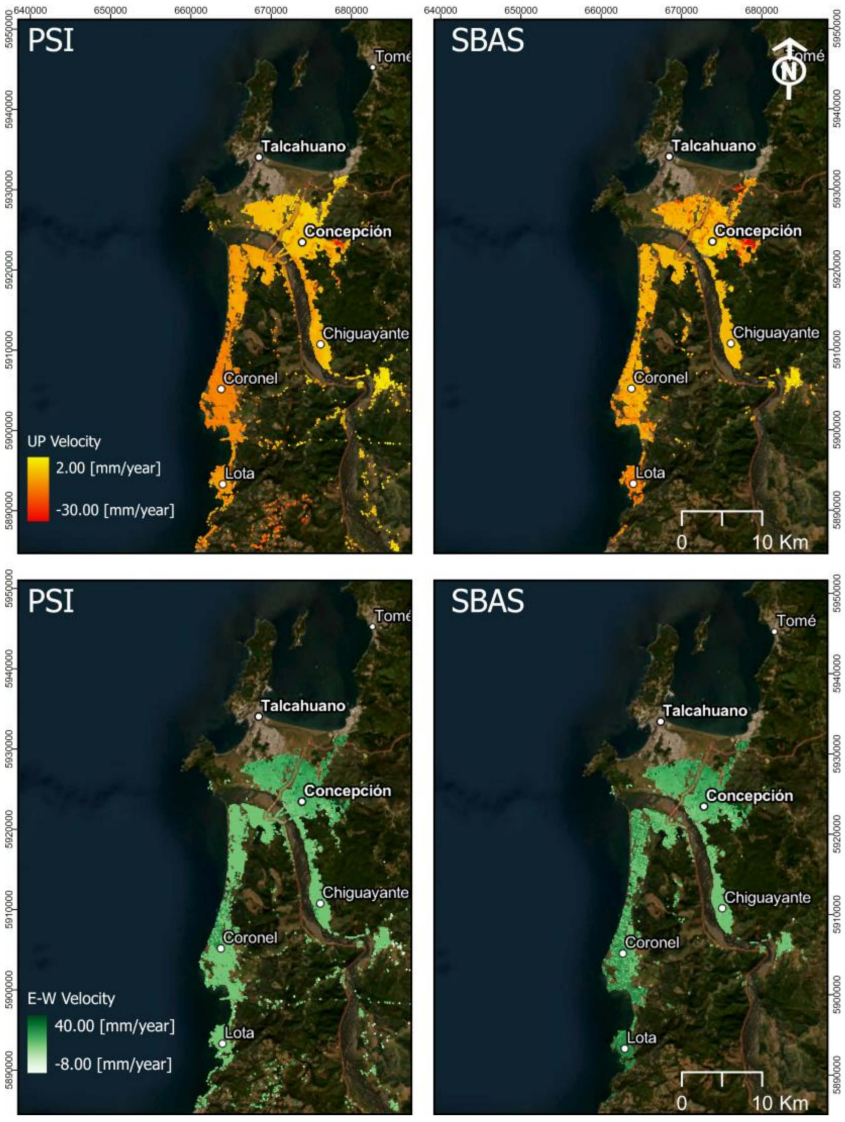

Figure 9. Vertical and horizontal (E-W) displacement in study area of Concepción, Chile.

The differences in the velocity trends between the obtained results from the two InSAR techniques are related to the backscatterers that fall within each grid cell whose velocities are averaged. Table 2 shows the statistics on the velocities found in the calibrated data and projected along the UP and N-E directions for the SBAS and PSI techniques over two differently resampled grids. The differences in the averaged velocities can be considered negligible since they are below the techniques' sensitivity. As expected, SBAS results shows a wider range of values because of its higher sensitivity over the considered grid.

Mean velocities values are consistent at the mm/year level, while it is possible to observe a wider range of values considering the SBAS approach, which likely allows us to better evidence local effects.

3.3. InSAR Deformation and Site Conditions

InSAR deformation in the basin of the city of Concepción is concentrated in a highly urbanized area, it has also been classified as a seismic zone due to a large magnitude earthquake, so it is very important to know the conditions of the site and compare them with the deformations of the land. The site condition in urban areas, located on an active subduction margin, constitute areas that are highly vulnerable to earthquakes. Many factors come into play in the stability of soil and structures due to deformations of the ground surface. In the case of seismic activity, the most important thing is the intensity of the ground movement, which determines quantitative values that allow for the estimation of possible damage to the infrastructure.

The surface geology of the urban center of the city of Concepción is mainly defined by Biobío Q1m sands with artificial deposits of CPg, characterized by low frequency (0.84 Hz) and high frequencies (2.50 to 3.46 Hz) calculated by HVSR (horizontal-to-vertical spectral ratio), as shown in Figure 10a. A clear peak is observed, suggesting an impedance contrast between the base rock and that the sedimentary fill, indicating soil stiffness, is more prone to compressibility. The Biobío Qtfb sands are fine-grained materials, with silt content to the south. The mixed fluvial deposits of the river are made up of fine- to medium-grained sands with abundant silts interspersed by various clay lenses and colluvial silts [65].

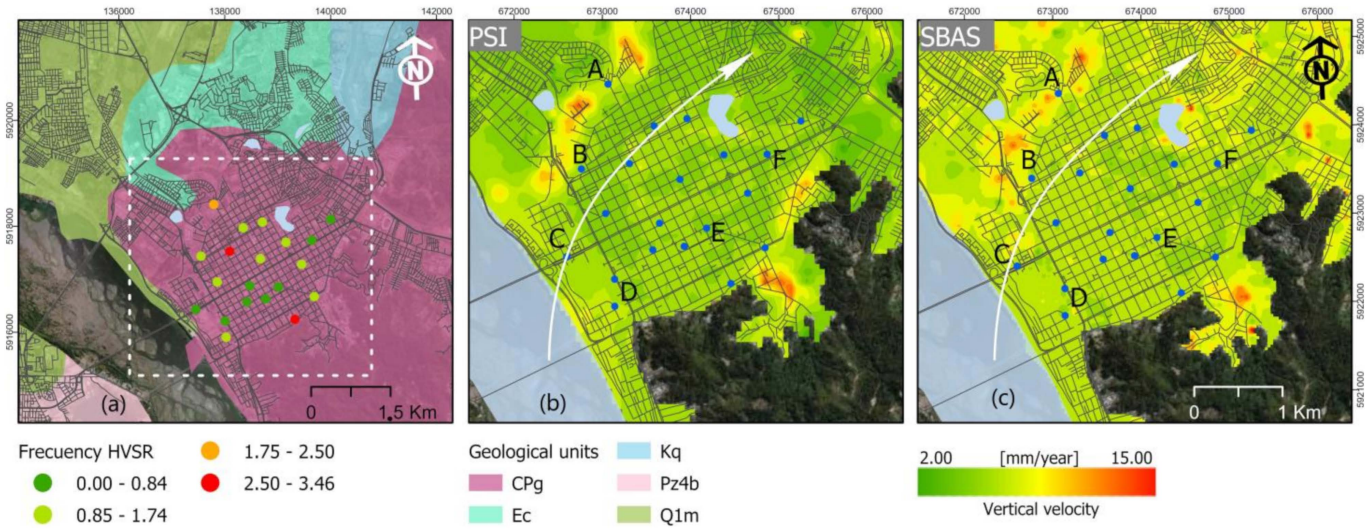

Figure 10. (**a**) HVSR measurement test, (**b**) PSI technique, and (**c**) SBAS technique. Blue dots are HVSR measurement points, and white arrow indicates water flow of Biobío delta river.

When analyzing Figure 10b,c, we note that the sites with previous measurements tend to coincide with low surface deformation, close to 2.00 mm/year. However, site A shows a relevant decrease in predominant frequency, which cannot be attributed to site surface changes due to the InSAR results, nor to a subsurface change because the material would need to have softened significantly which is highly unlikely. A plausible explanation is the neighboring sites to the NE and SW of Site A, as these do show an

important surface subsidence (higher than 10.00 mm/year). The surface settlement of the neighboring sites would decrease the confinement stresses on site A, thus decreasing its predominant frequency, which in turn would likely [65] increase its seismic demand on the next large seismic event.

The fundamental frequency (F0) appears as one of the indicators commonly used at a global level to evaluate the local effects that soils experience, this frequency (or period) represents the natural vibration of a site, allowing us to estimate the amplification or attenuation of seismic waves as they pass through different types of soils and rocks. During the period of April–May 2023, vibration measurements were taken in 20 sites, which already had f_0 measurements from 2011 following the Mw 8.8 2010 earthquake in the city of Concepción, where the following points stand out with their respective frequencies (Table 3). The HVSR samples were recorded for 40 min using a frequency of 512 Hz, the devices were in the direction of geographic north, avoiding bad weather conditions such as wind, heavy rain, and extreme temperatures. From the result obtained from values of fundamental frequencies, a comparison was carried out with data from samples collected in 2011 in the same sites, and thus, an evaluation was conducted to determine if changes occurred within each point. The data were processed in the open access software GEOPSY and then in a code created in MATLAB. The following table shows the fundamental frequency values obtained from some sectors and their difference after 12 years.

Table 3. Site conditions during HVSR test.

Points—Locations	F0_2011	F0_2023	Anomaly
A—Almirante RN	2.50	1.91	−0.59
B—Vicuna Mackena	1.00	0.90	−0.10
C—Carrera/Llacolen	0.83	0.89	0.06
D—Prat/O'higgins	0.71	0.75	0.04
E—Tribunales	0.77	0.81	0.04
F—Ainavillo	0.83	0.82	−0.01

Figure 11 shows the H/V ratios for site A (Almirante RN), where the highest difference is observed along with the H/V predominant frequency obtained in 2011. It is observed that they present varied values of frequency range for each place characterized by a wide site frequency (or predominant frequency) between 0.75 and 1.91 Hz, where the thick red line is the average of the horizontal components over the vertical, and the thinnest red lines are the values of the standard deviation. For sites A, a predominant frequency f_0 of 1.91 Hz is observed with an amplitude of 3.54, that is, greater than 2, suggesting an impedance contrast between the base rock and the sedimentary fill. On the other hand, sites B, C, D, and F present a clear peak with similar frequency values that agrees with their location at deeper parts of the Concepción basin [66]. In addition to presenting amplitudes close to 2, point E provides a curve that exhibits a peak of 1.81 amplitude, that is, less than 2, which may indicate a low impedance contrast. Comparing the HVSR values to the results provided for 2011, it is found that the Almirante RN site presents a decrease in the fundamental frequency value. Regarding the other sites, the dominant periods of the different locations are consistent with the values of previously proposed fundamental periods; that is, they do not present an important change for each location.

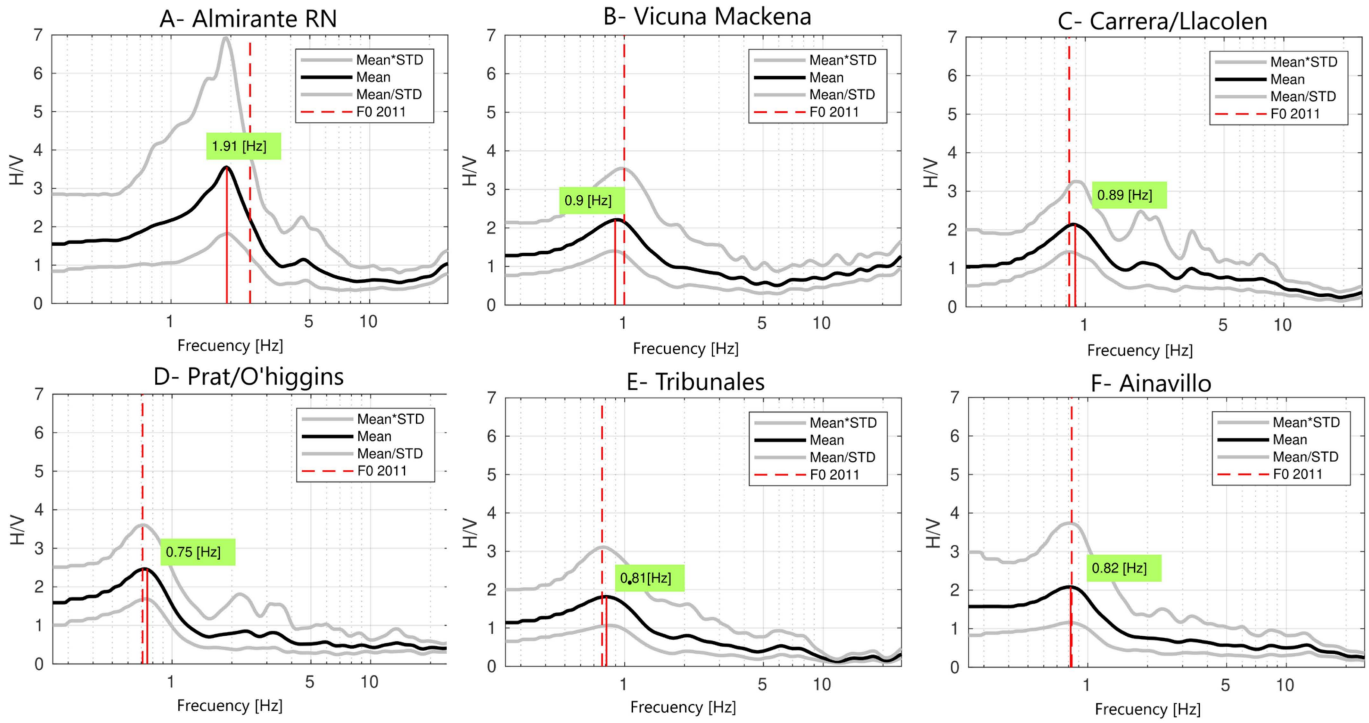

Figure 11. Test site conditions for point A, B, C, D, E, and F. Location is provided in Figure 10.

4. Conclusions

The results of the InSAR techniques have revealed local deformations, induced by natural and anthropogenic processes, determined mainly by the geological conditions of the site. However, there have been no major changes in site conditions following the large earthquakes that have affected the stability of the urban area. Measurements derived from the SBAS and PSI processing techniques applied to SAR data show common overall deformation rates. Local deformation patterns induced by alluvial sediment types can be observed. This allowed us to map basin deformations and investigate basin conditions, where no changes in site conditions have been evident in such a highly urbanized area that is typically exposed to seismic activity. Therefore, the study also confirms the effectiveness of SAR processing techniques, based on Sentinel-1 C-band images, for the Chilean region. Estimates of regional tectonic deformations will be evidenced in a future work using images from the Copernicus mission and by expanding the spatial coverage of the area of interest.

The comparison between the two InSAR datasets, using the SBAS and PSI techniques, shows a level of agreement in mm/year velocity rates, and their UP and East components. Both techniques allowed us to quantify the displacement relationship over areas affected by local subsidence within the urban center with high spatial resolution. On the other hand, the local soil subsidence obtained with the InSAR deformations should have a direct relationship with the soil rigidity, where the frequencies between measurements have decreased; conversely, soil flexibility should indicate an increase in site conditions between 2011 and 2023. However, a complete site analysis is necessary to determine the direct relationship between the InSAR data and site conditions, increasing the number of samples required to have a precise relationship between soil deformation and site conditions. This may open new fields of research for areas of high seismic activity.

Author Contributions: Conceptualization, E.G., F.O. and L.T.; methodology, F.O., E.G., L.T. and S.G.; SAR data processing, E.G. and F.O.; validation G.M., C.A. and M.M.; writing E.G., F.O., C.A. and G.M.; supervision, G.M., M.M. and S.G. All authors have read and agreed to the published version of the manuscript.

Funding: Supported by Chilean National Research and Development Agency, ANID/CONICYT, FONDECYT Postdoctoral ID: 3230061.

Data Availability Statement: The geological map is available on the portal of the National Geology and Mining Service (SERNAGEOMIN). The catalog of active failures is available at: https://fallasactivas.cl/ accessed on 10 September 2023, under license https://creativecommons.org/licenses/by/4.0/.

Acknowledgments: Acknowledgments go to the Chilean National Research and Development Agency, ANID/CONICYT, FONDECYT Postdoctoral ID: 3230061.

Conflicts of Interest: The authors declare no conflict of interest.

References

1. Assimaki, D.; Ledezma, C.; Montalva, G.A.; Tassara, A.; Mylonakis, G.; Boroschek, R. Site effects and damage patterns. *Earthq. Spectra* **2012**, *28* (Suppl. 1), 55–74. [CrossRef]
2. Bray, J.; Rollins, K.; Hutchinson, T.; Verdugo, R.; Ledezma, C.; Mylonakis, G.; Assimaki, D.; Montalva, G.; Arduino, P.; Olson, S.M.; et al. Effects of ground failure on buildings, ports, and industrial facilities. *Earthq. Spectra* **2012**, *28* (Suppl. 1), 97–118. [CrossRef]
3. Leyton, F.; Montalva, G.; Ramírez, P. Effects of surface geology on seismic motion. In Proceedings of the 4th IASPEI/IAEEE International Symposium, Santa Barbara, CA, USA, 23–26 August 2011; pp. 1–10.
4. Berardino, P.; Fornaro, G.; Lanari, R.; Sansosti, E. A new algorithm for surface deformation monitoring based on small baseline differential SAR interferograms. *IEEE Trans. Geosci. Remote Sens.* **2002**, *40*, 2375–2383. [CrossRef]
5. Ferretti, A.; Prati, C.; Rocca, F. Permanent scatterers in SAR interferometry. *IEEE Trans. Geosci. Remote Sens.* **2001**, *39*, 8–20. [CrossRef]
6. Bonano, M.; Manunta, M.; Pepe, A.; Paglia, L.; Lanari, R. From previous C-band to new X-band SAR systems: Assessment of the DInSAR mapping improvement for deformation time-series retrieval in urban areas. *IEEE Trans. Geosci. Remote Sens.* **2013**, *51*, 1973–1984. [CrossRef]
7. Casu, F.; Manzo, M.; Lanari, R. A quantitative assessment of the SBAS algorithm performance for surface deformation retrieval from DInSAR data. *Remote Sens. Environ.* **2006**, *102*, 195–210. [CrossRef]
8. Li, Z.; Wen, Y.; Zhang, P.; Liu, Y.; Zhang, Y. Joint investment of GPS, leveling, and InSAR data for the 2013 Lushan (China) earthquake and its seismic hazard implications. *Remote Sens.* **2020**, *12*, 715. [CrossRef]
9. Weston, J.; Ferreira, A.M.; Funning, G.J. Systematic comparisons of earthquake source models determined using InSAR and seismic data. *Tectonophysics* **2012**, *532*, 61–81. [CrossRef]
10. Orellana, F.; Hormazábal, J.; Montalva, G.; Moreno, M. Measuring Coastal Subsidence after Recent Earthquakes in Central Chile Using SAR Interferometry and GNSS Data. *Remote Sens.* **2022**, *14*, 1611. [CrossRef]
11. Van Natijne, A.L.; Bogaard, T.A.; van Leijen, F.J.; Hanssen, R.F.; Lindenbergh, R.C. World-wide InSAR sensitivity index for landslide deformation tracking. *Int. J. Appl. Earth Obs. Geoinf.* **2022**, *111*, 102829. [CrossRef]
12. Fobert, M.A.; Singhroy, V.; Spray, J.G. InSAR monitoring of landslide activity in Dominica. *Remote Sens.* **2021**, *13*, 815. [CrossRef]
13. Orellana, F.; Moreno, M.; Yáñez, G. High-Resolution Deformation Monitoring from DInSAR: Implications for Geohazards and Ground Stability in the Metropolitan Area of Santiago, Chile. *Remote Sens.* **2022**, *14*, 6115. [CrossRef]
14. Bonì, R.; Herrera, G.; Meisina, C.; Notti, D.; Béjar-Pizarro, M.; Zucca, F.; Gonzalez, P.J.; Palano, M.; Tomás, R.; Fernandez, J.; et al. Twenty-year advanced DInSAR analysis of severe land subsidence: The Alto Guadalentín Basin (Spain) case study. *Eng. Geol.* **2015**, *198*, 40–52. [CrossRef]
15. Ezquerro, P.; Tomás, R.; Béjar-Pizarro, M.; Fernández-Merodo, J.A.; Guardiola-Albert, C.; Staller, A.; Sánchez-Sobrino, J.A.; Herrera, G. Improving multi-technique monitoring using Sentinel-1 and Cosmo-SkyMed data and upgrading groundwater model capabilities. *Sci. Total Environ.* **2020**, *703*, 134757. [CrossRef] [PubMed]
16. Orellana, F.; Rivera, D.; Montalva, G.; Arumi, J.L. InSAR-Based Early Warning Monitoring Framework to Assess Aquifer Deterioration. *Remote Sens.* **2023**, *15*, 1786. [CrossRef]
17. Chang, L.; Dollevoet, R.P.; Hanssen, R.F. Monitoring line-infrastructure with multisensor SAR interferometry: Products and performance assessment metrics. *IEEE J. Sel. Top. Appl. Earth Obs. Remote Sens.* **2018**, *11*, 1593–1605. [CrossRef]
18. De Corso, T.; Mignone, L.; Sebastianelli, A.; del Rosso, M.; Yost, C.; Ciampa, E.; Pecce, M.; Sica, S.; Ullo, S. Application of DInSAR technique to high coherence satellite images for strategic infrastructure monitoring. In Proceedings of the IGARSS 2020–2020 IEEE International Geoscience and Remote Sensing Symposium, Waikoloa, HI, USA, 26 September–2 October 2020; IEEE: New York, NY, USA, 2020; pp. 4235–4238.
19. Orellana, F.; Delgado Blasco, J.M.; Foumelis, M.; D'Aranno, P.J.; Marseille, M.A.; Di Mascio, P. Dinsar for road infrastructure monitoring: Case study highway network of Rome metropolitan (Italy). *Remote Sens.* **2020**, *12*, 3697. [CrossRef]
20. Orellana, F.; D'Aranno, P.J.; Scifoni, S.; Marsella, M. SAR Interferometry Data Exploitation for Infrastructure Monitoring Using GIS Application. *Infrastructures* **2023**, *8*, 94. [CrossRef]
21. Ho Tong Minh, D.; Hanssen, R.; Rocca, F. Radar interferometry: 20 years of development in time series techniques and future perspectives. *Remote Sens.* **2020**, *12*, 1364. [CrossRef]

22. Ferretti, A.; Prati, C.; Rocca, F. Nonlinear subsidence rate estimation using permanent scatterers in differential SAR interferometry. *IEEE Trans. Geosci. Remote Sens.* **2000**, *38*, 2202–2212. [CrossRef]
23. Hooper, A.; Zebker, H.; Segall, P.; Kampes, B. A new method for measuring deformation on volcanoes and other natural terrains using InSAR persistent scatterers. *Geophys. Res. Lett.* **2004**, *31*. [CrossRef]
24. Van der Kooij, M.; Lacoste, H. Coherent target analysis. In Proceedings of the Third International Workshop on ERS SAR Interferometry (FRINGE 2003), Frascati, Italy, 20 August 2003; pp. 2–5.
25. Kampes, B.M. *Radar Interferometry*; Springer: Dordrecht, The Netherlands, 2006; Volume 12.
26. Costantini, M.; Falco, S.; Malvarosa, F.; Minati, F. A new method for identification and analysis of persistent scatterers in series of SAR images. In Proceedings of the IGARSS 2008–2008 IEEE International Geoscience and Remote Sensing Symposium, Boston, MA, USA, 6–11 July 2008; IEEE: New York, NY, USA; Volume 2, pp. II-449–II-452.
27. Perissin, D.; Wang, T. Repeat-pass SAR interferometry with partially coherent targets. *IEEE Trans. Geosci. Remote Sens.* **2011**, *50*, 271–280. [CrossRef]
28. Devanthéry, N.; Crosetto, M.; Monserrat, O.; Cuevas-González, M.; Crippa, B. An approach to persistent scatterer interferometry. *Remote Sens.* **2014**, *6*, 6662–6679. [CrossRef]
29. Lanari, R.; Mora, O.; Manunta, M.; Mallorquí, J.J.; Berardino, P.; Sansosti, E. A small-baseline approach for investigating deformations on full-resolution differential SAR interferograms. *IEEE Trans. Geosci. Remote Sens.* **2004**, *42*, 1377–1386. [CrossRef]
30. Hong, S.H.; Wdowinski, S.; Kim, S.W.; Won, J.S. Multi-temporal monitoring of wetland water levels in the Florida Everglades using interferometric synthetic aperture radar (InSAR). *Remote Sens. Environ.* **2010**, *114*, 2436–2447. [CrossRef]
31. Hetland, E.A.; Musé, P.; Simons, M.; Lin, Y.N.; Agram, P.S.; DiCaprio, C.J. Multiscale InSAR time series (MINTS) analysis of surface deformation. *J. Geophys. Res. Solid Earth* **2012**, 117. [CrossRef]
32. Yunjun, Z.; Fattahi, H.; Amelung, F. Small baseline InSAR time series analysis: Unwrapping error correction and noise reduction. *Comput. Geosci.* **2019**, *133*, 104331. [CrossRef]
33. Casu, F.; Elefante, S.; Imperatore, P.; Zinno, I.; Manunta, M.; De Luca, C.; Lanari, R. SBAS-DInSAR parallel processing for deformation time-series computation. *IEEE J. Sel. Top. Appl. Earth Obs. Remote Sens.* **2014**, *7*, 3285–3296. [CrossRef]
34. Manunta, M.; De Luca, C.; Zinno, I.; Casu, F.; Manzo, M.; Bonano, M.; Fusco, A.; Pepe, A.; Onorato, G.; Berardino, P.; et al. The parallel SBAS approach for Sentinel-1 interferometric wide swath deformation time-series generation: Algorithm description and products quality assessment. *IEEE Trans. Geosci. Remote Sens.* **2019**, *57*, 6259–6281. [CrossRef]
35. Torres, R.; Snoeij, P.; Geudtner, D.; Bibby, D.; Davidson, M.; Attema, E.; Potin, P.; Rommen, B.; Floury, N.; Brown, M.; et al. GMES Sentinel-1 mission. *Remote Sens. Environ.* **2012**, *120*, 9–24. [CrossRef]
36. De Zan, F.; Guarnieri, A.M. TOPSAR: Terrain observation by progressive scans. *IEEE Trans. Geosci. Remote Sens.* **2006**, *44*, 2352–2360. [CrossRef]
37. Cigna, F.; Esquivel Ramírez, R.; Tapete, D. Accuracy of Sentinel-1 PSI and SBAS InSAR Displacement Velocities against GNSS and Geodetic Leveling Monitoring Data. *Remote Sens.* **2021**, *13*, 4800. [CrossRef]
38. Adam, N.; Parizzi, A.; Eineder, M.; Crosetto, M. Practical persistent scatterer processing validation in the course of the Terrafirma project. *J. Appl. Geophys.* **2009**, *69*, 59–65. [CrossRef]
39. Cigna, F.; Sowter, A. The relationship between intermittent coherence and precision of ISBAS InSAR ground motion velocities: ERS-1/2 case studies in the UK. *Remote Sens. Environ.* **2017**, *202*, 177–198. [CrossRef]
40. Pepe, A. Multi-temporal small baseline interferometric SAR algorithms: Error budget and theoretical performance. *Remote Sens.* **2021**, *13*, 557. [CrossRef]
41. Moreno, M.; Melnick, D.; Rosenau, M.; Baez, J.; Klotz, J.; Oncken, O.; Tassara, A.; Chen, J.; Bataille, K.; Bevis, M.; et al. Toward understanding tectonic control on the Mw 8.8 2010 Maule Chile earthquake. *Earth Planet. Sci. Lett.* **2012**, *321*, 152–165. [CrossRef]
42. Yáñez-Cuadra, V.; Moreno, M.; Ortega-Culaciati, F.; Donoso, F.; Báez, J.C.; Tassara, A. Mosaicking Andean morphostructure and seismic cycle crustal deformation patterns using GNSS velocities and machine learning. *Front. Earth Sci.* **2023**, *11*, 1096238. [CrossRef]
43. SERNAGEOMN—National Geology and Mining Service, Source Open Geological Map of Chile. Available online: https://www.sernageomin.cl/geologia/ (accessed on 15 May 2023).
44. Montalva, G.A.; Chávez-Garcia, F.J.; Tassara, A.; Jara Weisser, D.M. Site effects and building damage characterization in Concepción after the Mw 8.8 Maule earthquake. *Earthq. Spectra* **2016**, *32*, 1469–1488. [CrossRef]
45. Galli, C. Geología urbana y suelos de fundación de Concepción y Talcahuano. In *Informe Final del Proyecto de Investigación N°75 de la Comisión de Investigación Científica de la Universidad de Concepción*; Universidad de Concepción: Concepción, Chile, 1967. (In Spanish)
46. Vivallos, J.; Ramírez, P.Y.; Fonseca, A. *Microzonificación Sísmica de la Ciudad de Concepción, Región del Biobío. Servicio Nacional de Geología y Minería. Carta Geológica de Chile, Serie Geológica Ambiental X. 3 Mapa Escala 1:20.000*; Servicio Nacional de Geología y Minería: Santiago, Chile, 2009.
47. Xu, B.; Li, Z.; Zhu, Y.; Shi, J.; Feng, G. Kinematic coregistration of sentinel-1 TOPSAR images based on sequential least squares adjustment. *IEEE J. Sel. Top. Appl. Earth Obs. Remote Sens.* **2020**, *13*, 3083–3093. [CrossRef]
48. Foumelis, M.; Blasco, J.M.D.; Desnos, Y.L.; Engdahl, M.; Fernández, D.; Veci, L.; Lu, J.; Wong, C. ESA SNAP-StaMPS integrated processing for Sentinel-1 persistent scatterer interferometry. In Proceedings of the IGARSS 2018–2018 IEEE International Geoscience and Remote Sensing Symposium, Valencia, Spain, 22–27 July 2018; IEEE: New York, NY, USA, 2018; pp. 1364–1367.

49. Hooper, A.; Spaans, K.; Bekaert, D.; Cuenca, M.C.; Arıkan, M.; Oyen, A. *StaMPS/MTI Manual*; Delft Institute of Earth Observation and Space Systems Delft University of Technology: Delft, The Netherlands, 2010; Volume 1, p. 2629.
50. Hooper, A.; Segall, P.; Zebker, H. Persistent Scatterer Interferometric Synthetic Aperture Radar for Crustal Deformation Analysis, with applications to Volcàn Alcedo. *J. Geophys. Res.* **2007**, *112*. [CrossRef]
51. Delgado Blasco, J.M.; Foumelis, M.; Stewart, C.; Hooper, A. Measuring urban subsidence in the Rome metropolitan area (Italy) with Sentinel-1 SNAP-StaMPS persistent scatterer interferometry. *Remote Sens.* **2019**, *11*, 129. [CrossRef]
52. Lanari, R.; Casu, F.; Manzo, M.; Zeni, G.; Berardino, P.; Manunta, M.; Pepe, A. An overview of the small baseline subset algorithm: A DInSAR technique for surface deformation analysis. In *Deformation and Gravity Change: Indicators of Isostasy Tectonics, Volcanism, and Climate Change*; Birkhäuser: Basel, Switzerland, 2007; pp. 637–661.
53. Zebker, H.A.; Villasenor, J. Decorrelation in interferometric radar echoes. *IEEE Trans. Geosci. Remote Sens.* **1992**, *30*, 950–959. [CrossRef]
54. De Luca, C.; Bonano, M.; Casu, F.; Fusco, A.; Lanari, R.; Manunta, M.; Pepe, A.; Zinno, I. Automatic and systematic Sentinel-1 SBAS-DInSAR processing chain for deformation time-series generation. *Procedia Comput. Sci.* **2016**, *100*, 1176–1180. [CrossRef]
55. Zinno, I.; Casu, F.; De Luca, C.; Elefante, S.; Lanari, R.; Manunta, M. A cloud computing solution for the efficient implementation of the P-SBAS DInSAR approach. *IEEE J. Sel. Top. Appl. Earth Obs. Remote Sens.* **2016**, *10*, 802–817. [CrossRef]
56. Imperatore, P.; Pepe, A.; Sansosti, E. High performance computing in satellite SAR interferometry: A critical perspective. *Remote Sens.* **2021**, *13*, 4756. [CrossRef]
57. De Luca, C.; Cuccu, R.; Elefante, S.; Zinno, I.; Manunta, M.; Casola, V.; Rivolta, G.; Lanari, R.; Casu, F. An On-Demand Web Tool for the Unsupervised Retrieval of Earth's Surface Deformation from SAR Data: The P-SBAS Service within the ESA G-POD Environment. *Remote Sens.* **2015**, *7*, 15630–15650. [CrossRef]
58. SONEL Serves as the GNSS Data Assembly Centre for the Global Sea Level Observing System (GLOSS); p. 61. Available online: https://www.sonel.org/spip.php?page=gps&idStation=4491 (accessed on 1 June 2023).
59. The International Terrestrial Reference Frame (ITRF). Available online: https://www.iers.org/IERS/EN/DataProducts/ITRF/itrf.html (accessed on 1 June 2023).
60. Catalão, J.; Nico, G.; Hanssen, R.; Catita, C. Integration of InSAR and GPS for vertical deformation monitoring: A case of study in Faial and Pico Islands. In Proceedings of the Fringe 2009 Workshop, Frascati, Italy, 30 November–4 December 2009.
61. Samsonov, S.; Tiampo, K. Analytical optimization of a DInSAR and GPS dataset for derivation of three-dimensional surface motion. *IEEE Geosci. Remote Sens. Lett.* **2006**, *3*, 107–111. [CrossRef]
62. Fuhrmann, T.; Garthwaite, M.C. Resolving three-dimensional surface motion with InSAR: Constraints from multi-geometry data fusion. *Remote Sens.* **2019**, *11*, 241. [CrossRef]
63. Cigna, F.; Tapete, D. Sentinel-1 big data processing with P-SBAS InSAR in the geohazards exploitation platform: An experiment on coastal land subsidence and landslides in Italy. *Remote Sens.* **2021**, *13*, 885. [CrossRef]
64. Link, O.; Brox-Escudero, L.M.; González, J.; Aguayo, M.; Torrejón, F.; Montalva, G.; Eguibar-Galán, M.Á. A paleo-hydro-geomorphological perspective on urban flood risk assessment. *Hydrol. Process.* **2019**, *33*, 3169–3183. [CrossRef]
65. Leyton, F.; Sepúlveda, S.A.; Astroza, M.; Rebolledo, S.; Acevedo, P.; Ruiz, S.; Gonzalez, L.; Foncea, C. Seismic zonation of the Santiago Basin, Chile. In Proceedings of the Fifth International Conference on Earthquake Geotechnical Engineering 2011, Santiago, Chile, 10–13 January 2011.
66. Montalva, G.A.; Bastías, N.; Leyton, F. Strong ground motion prediction model for PGV and spectral velocity for the Chilean subduction zone. *Bull. Seismol. Soc. Am.* **2022**, *112*, 348–360. [CrossRef]